

Hybrid organic-inorganic nanotubes effectively adsorb some organic pollutants in aqueous phase

Roberto Nasi, Filomena Sannino, Pierre Picot, Antoine Thill, Olimpia Oliviero, Serena Esposito, Marco Armandi, Barbara Bonelli

▶ **To cite this version:**

Roberto Nasi, Filomena Sannino, Pierre Picot, Antoine Thill, Olimpia Oliviero, et al.. Hybrid organic-inorganic nanotubes effectively adsorb some organic pollutants in aqueous phase. Applied Clay Science, 2020, 186, pp.105449. 10.1016/j.clay.2020.105449 . cea-02458782

HAL Id: cea-02458782

https://cea.hal.science/cea-02458782

Submitted on 21 Jul 2022

HAL is a multi-disciplinary open access archive for the deposit and dissemination of scientific research documents, whether they are published or not. The documents may come from teaching and research institutions in France or abroad, or from public or private research centers.

L'archive ouverte pluridisciplinaire **HAL**, est destinée au dépôt et à la diffusion de documents scientifiques de niveau recherche, publiés ou non, émanant des établissements d'enseignement et de recherche français ou étrangers, des laboratoires publics ou privés.



Distributed under a Creative Commons Attribution - NonCommercial 4.0 International License

Version of Record: https://www.sciencedirect.com/science/article/pii/S0169131720300144
Manuscript_ddadb80d667bad1b8eb43a29b89bfacf

Hybrid organic-inorganic nanotubes effectively adsorb some organic pollutants in aqueous phase

Roberto Nasi,[1,§] Filomena Sannino,[2] Pierre Picot,[3,§] Antoine Thill,[3] Olimpia Oliviero,[4] Serena Esposito,[1] Marco Armandi,[1] Barbara Bonelli[1,*]

[1]*LIONS, NIMBE, CEA, CNRS, Université Paris-Saclay, CEA-Saclay, Gif-sur-Yvette, 91191, France*

[2]*Department of Agricultural Sciences– Università degli Studi di Napoli Federico II, 80055 Portici-Napoli, Italy*

[3]*Department of Applied Science and Technology & INSTM Unit of Torino Politecnico - Politecnico di Torino, 10129 Torino, Italy*

[4]*Department of Neuroscience and Reproductive and Odontostomatologic Sciences, Università degli Studi di Napoli Federico II, 80055 Portici- Napoli, Italy*

Keywords: imogolite; SAXS; hybrid nanotubes; MCPA; herbicides; dichloromethane

Corresponding author: *barbara.bonelli@polito.it

§ Both authors equally contributed to the paper.

© 2020 published by Elsevier. This manuscript is made available under the CC BY NC user license
https://creativecommons.org/licenses/by-nc/4.0/

Abstract

Methylimogolite nanotubes (Me-IMO NTs, chemical composition $(OH)_3Al_2O_3SiCH_3$) are characterized by having an inner hydrophobic (fully-methylated) surface. Conversely, the outer surface is hydrophilic and positively charged below the point of zero charge (at pH = 8.6), due to the $Al(OH)Al + H^+ = Al(OH)_2^+Al$ equilibrium occurring at the outer surface of the NTs when they are dispersed in water.

In this work, adsorption of MCPA (2-methyl-4-chlorophenoxyacetic acid) and of dichloromethane (DCM) on Me-IMO NTs was studied by means of both adsorption/desorption measurements in batch conditions (at room temperature and at different pH value) and Small Angle X-rays Scattering (SAXS).

MCPA, which partially dissociates in water (pK_a = 2.90), is mainly adsorbed at the outer surface of the NTs, although measurements in batch conditions show that other types of interaction occur (i.e. H-bond) at higher MCPA concentration. SAXS measurements confirm that MCPA has not entered the NTs inner pores.

Interaction of the NTs with DCM, instead, is more complex: SAXS measurements show that DCM molecules interact with the NTs inner surface, whereas batch experiments indicate that additional interactions take place with the outer surface of the NTs.

Introduction

Hybrid organic-inorganic nanotubes (NTs) with chemical formula $(OH)_3Al_2O_3SiCH_3$ (Me-IMO) can be synthesized in water by a template-free sol-gel procedure, starting from commercial precursors, i.e. an Al salt (or alkoxide) and triethoxymethylsilane (TEMS) (Bottero et al., 2011). Dual functionalization of the inner surface is also possible to a certain extent (Picot et al., 2019) and Ge-analogues can be obtained, as well (Amara et al., 2015).

Me-IMO NTs have unique properties: they are mainly mesoporous with remarkably high accessible specific surface area (about 650 m^2 g^{-1}) and are thermally stable up to 300 °C (Mackenzie, 1989; Bottero et al., 2011). When dispersed in water, the NTs are positively charged at pH values below 9 (Bahadori et al., 2018). Such positive charge stems, in part, from the acid-base properties of external -OH groups (Gustafsson, 2001) as in eq. (1):

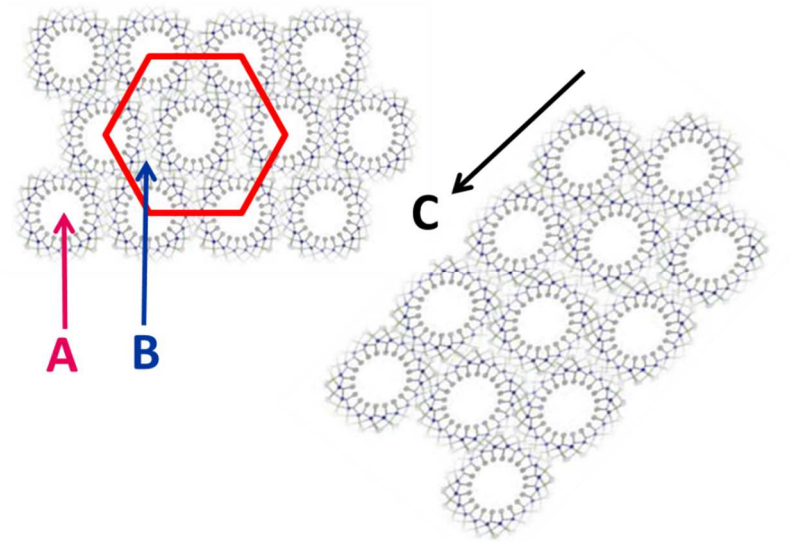
$$Al(OH)Al + H^+ = Al(OH)_2^+Al \qquad (1)$$

and, in part, from some curvature effects (Poli et al., 2015).

Proper (inorganic) imogolite (IMO) NTs (Cradwick et al., 1972), which can be obtained by sol-gel methods as well (Du et al., 2017), have different structure (Thill et al., 2017) and applications, depending on whether they occur as a powder or in aqueous suspension of freshly synthesized NTs. Aqueous dispersions of pristine IMO NTs, which have never been dried, do not show any bundles, since the NTs repeal each other, due to their positive surface charge. The NTs may form bundles upon addition of salt or upon increase of pH. In such a case, bundles formation is irreversible to a large extent (Karube, 1998).

Surprisingly, even in freshly synthesized dispersions, Me-IMO NTs are always observed to form bundles (Scheme 1), where three types of pores A, B and C can be identified (Ackerman et al., 1993). Noticeably, in Me-IMO the A pores have an average diameter of 2.0 nm and are extremely hydrophobic, whereas in IMO they have an average diameter of 1.0 nm and are extremely

hydrophilic (Bonelli et al., 2009; Zanzottera et al., 2012b); the B pores are 0.45 nm wide in Me-IMO, allowing adsorption of small probes in gas/solid systems (Zanzottera et al., 2012a; Bonelli et al., 2013a), being instead smaller in IMO (*ca.* 0.30 nm) and, thus, less accessible to gas probes (Ackerman et al., 1993). Finally, the C pores (Scheme 1) are larger slit-mesopores, accessible to large molecules (Garrone and Bonelli, 2016; Shafia et al., 2016a) and characterized by amphoteric properties (Bonelli et al., 2009, 2013b) in both Me-IMO and IMO.



Scheme 1.

Three types of pores occurring in Me-IMO NTs in the powder form.

Although also gels may be obtained, usually powders of Me-IMO NTs are obtained (Bottero et al., 2011). In water, the positively charged outer surface (eq. 1) favours both NTs re-dispersion, and interaction with negatively charged species (Bonelli, 2016) and/or polar molecules (Boyer et al., 2014). Nonetheless, some of us showed that in oil-in-water emulsion, Me-IMO NTs adsorb at the oil/water interface, stabilizing the emulsion by inducing slow oil-triggered modifications of the viscosity of the continuous phase and, possibly, favouring transport of small molecules within the NTs (Picot et al., 2016).

With Me-IMO NTs, the simultaneous occurrence of an inner hydrophobic surface and an outer hydrophilic (and positively charged surface) may be of interest in applications implying

selective adsorption, like gas membranes, adsorption of complex mixtures and removal of water pollutants, as well. Indeed, IMO has been proposed as an optimal adsorbent of anions and, in particular, for phosphate fixation at the outer surface of the NTs (Mizota, 1977; Parfitt, 2009; Rojas-Mancilla et al., 2019).

There is currently a great interest into the development of new nanomaterials able to efficiently remove from water several organic pollutants, besides inorganic ones, like agrochemicals, dyes, halogenated compounds, pharmaceutical and personal care products, etc. (Freyria et al., 2018). Some of us studied the adsorption and degradation of the azo-dye Acid Orange 7 (AO7, $C_{16}H_{11}N_2SO_4Na$) in the presence of aqueous suspensions of IMO, Me-IMO or Fe^{3+}-doped NTs (Shafia et al., 2016a; Bahadori et al., 2018). Some interesting insights were obtained, like the preferential interaction of AO7 moieties (negatively charged in water) with the outer surface of NTs, although some of the inner Si-OH groups of IMO NTs (likely those at the mouth of A pores) were able to interact with the pollutant by H-boding. In the presence of Fe^{3+}species, instead, a ligand displacement phenomenon was observed, where Fe^{3+} ions were able to coordinate the dye through its N atoms. (Shafia et al., 2016a). This work focuses, instead, on the interaction of Me-IMO NTs with two organic molecules (Table 1) in water suspension, namely 4-chloro-2-methylphenoxyacetic acid (MCPA) and dichloromethane (DCM).

Table 1

Some properties of MCPA and DCM.

Pollutant	Molecule dimension(s) (nm)	Dipole Moment (D)	pKa	Solubility in water (g/L)	Bulk Electron density ($e^-/Å^3$)
MCPA	~ 0.8 x 0.7		2.90	0.825 at 23 °C[b]	0.480
DCM	0.33[a]	1.470	-	17.5 at 25 °C	0.396

[a]Kinetic diameter
[b] (Gimeno et al., 2003)

MCPA is a phenoxy herbicide extensively used in agriculture to control annual and perennial weeds in cereals, grasslands, trees and turf: being highly soluble in water and very mobile,

it can leach from soil and can be found in groundwater wells, thus posing serious environmental problems. For this reason, the U.S. Environmental Protection Agency (EPA) classifies MCPA as a potential groundwater contaminant (Addorisio et al., 2010).

DCM is a chlorinated volatile organic compound (VOC), which is soluble in water due to its dipole moment (μ_{DCM} = 1.470 D): it is manly used as solvent and reagent, being also employed in the manufacture of aerosols, adhesives, and for dry cleaning (Huang et al., 2014). In addition to its high toxicity and carcinogenic character, DCM contributes to global warming, depletion of the ozone layer, and photochemical smog: the U.S. EPA has included it among the 17 highly dangerous chemicals that should be targeted for emissions reduction.

In this work, a sample of Me-IMO NTs was characterized by powder X-ray Diffraction (XRD), N_2 isotherms at -196 °C, ζ-potential measurements and SAXS and was tested as adsorbent of either MCPA or DCM by means of adsorption/desorption experiments in batch conditions and by SAXS.

2. Materials and Methods

2.1 Me-IMO synthesis

A sample of Me-IMO was synthesized according to a procedure reported elsewhere (Bottero et al., 2011). In acidic medium due to $HClO_4$, Al-*sec*-butoxide (ASB) and triethoxymethylsilane (TEMS) were used as the Al and Si source, respectively, with molar ratio Al : Si = 2 : 1.15. The slight excess of TEMS was used to prevent formation of by-products (i.e. Al hydroxide) due to fast hydrolysis of ASB, which is a crucial issue in the synthesis. For the same reason, the sample was synthesised in a dry room (i.e. a moisture-free environment) (Shafia et al., 2016b).

2.2. Me-IMO characterization

X-ray powder diffraction (XRD) were measured in the 2.5–20° 2θ range on an 'Xpert Diffractometer (Cu K_α radiation; l=1.5414 Å, step width = 0.02 2θ).

The values of BET SSA (Brunauer Emmett Teller Specific Surface Area), total pore volume and *t-plot* microporous volume reported in Table 2 were calculated from the N_2 adsorption/desorption isotherm measured at -196 °C on the powder outgassed at 275 °C in order to remove residual water and atmospheric contaminants. The Non Local-Density Function Theory Pore Size Distribution (NL-DFT PSD) and the corresponding cumulative pore volume curve were obtained by applying a N_2–silica kernel (for cylindrical pores) to the isotherm adsorption branch.

The Al/Si ratio was measured by means of Energy Dispersive X-ray analysis (EDX, AZTec, Oxford Instruments) on three different spots (ca. 0.1 mm^2 area each): the so-obtained average value Al/Si = 0.49 was in fair agreement with the theoretical one Al/Si = 0.50.

Electrophoretic mobility as a function of pH was measured at 25°C by means of light scattering technique on a Zetasizer Nano-ZS instrument (Malvern Instruments, Worcestershire, UK). The corresponding ζ-potential curve was calculated according to the Henry's equation $UE= 2\varepsilon\zeta f(Ka)/3\eta$, where UE is the electrophoretic mobility, ε is the dielectric constant, ζ is the zeta potential, f(Ka) is the Henry's function, and η is the viscosity. The adopted value of f(Ka) was 1.5, in agreement with the Smoluchowski approximation, usually applied to aqueous solutions of moderate electrolyte concentration, as in the present case. Water suspensions were obtained after 2 min sonication with an ultrasonic probe (100 W,20 kHz, Sonoplus; Bandelin, Berlin, Germany); the pH of the suspension was then adjusted by adding either 0.10 M HCl or 0.10 MNaOH.

SAXS (Small Angle X-ray Scattering) data were acquired on a Xeuss 2.0 HR SAXS/WAXS instrument (Xenocs) equipped with a microfocus Copper sealed tube (30 W/30 μm) ; single reflection multilayer optic with 2D collimation for Cu Kα (λ=1.5414 Å) and 2 motorized scatter-less slits 2.0 with variable aperture enable the definition of the beam energy (Cu Kα with spectral purity > 97 %) and size while minimizing the scattering background. The divergence of the beam is < 0.4 mrad in both planes perpendicular to beam axis. The sample were measure in the high resolution beam configuration with a max flux at the sample position of $1x10^8$ (ph/s).

174 Me-IMO NTs were studied both as powder and in water suspension: in the former case, the
175 powder was fixed between two Kapton films and placed in aluminium frame (Fig. 6), whilst glass
176 capillaries containing dispersion and contaminants were vacuum tight sealed and placed in a
177 different aluminium sample holder that can accommodate up to 20 capillaries.
178 MCPA adsorption on MeIMO has been evaluated by SAXS, as follows: a stock dispersion
179 of 5g/L of MeIMO in 100μM of herbicide water (MilliQ) solution was prepared (natural pH 4.45).
180 From the stock MeIMO dispersion three samples were also prepared at different pH (3, 4.45, 9.65,
181 10.46) by means of HCl or NH_3 addition.
182 DCM adsorption on Me-IMO has been evaluated by SAXS at natural pH.
183
184 *2.3 Adsorption/desorption experiment in batch-conditions*
185 4-chloro-2-methylphenoxyacetic acid (MCPA) and Dichloromethane (DCM) were
186 purchased from Sigma-Aldrich Chemical Co. (Poole, Dorset, U.K.; 99.0% purity). HPLC grade
187 solvents (Carlo Erba, Milan, Italy) were used without further purification. All the other chemicals
188 were from Sigma-Aldrich, unless otherwise specified.
189 For MCPA experiments, a stock solution of the herbicide was prepared by dissolving 200
190 mg MCPA in 1000 mL of ultrapure water (final concentration 1000 μmol L^{-1}) and, then, kept
191 refrigerated.
192 For DCM experiments, a stock solution of the organic pollutant was prepared by diluting
193 DCM with ultrapure water (final concentration 0.15 mol L^{-1}).
194
195 *2.3.1 Analytical determination of the organic contaminants*
196 The concentration of MCPA was measured on an Agilent 1200 Series HPLC apparatus
197 (Wilmington, DE), equipped with a DAD array and a ChemStation Agilent Software. A Macharey-
198 Nagel Nucleosil 100-5 C18 column (stainless steel 250 4 mm) was used.

For MCPA determination, the mobile phase, comprising a binary system of 50:50 acetonitrile: phosphate buffer (0.1%, pH 2.5), was pumped at 1 mL min^{-1} flow in isocratic mode. The UV detector was set at 225 nm. The quantitative determination of MCPA was performed by elaborating its corresponding calibration curve in the 0.25 - 1000 μmol L^{-1} range.

The concentration of DCM was determined by Gas Chromatography-Mass Spectrometry (GC-MS). The samples were analysed on a Perkin-Elmer AutoSystemTMXL GC, equipped with a Programmed-Temperature Split/Splitless injector with programmable pneumatic control kept at a constant temperature of 250 °C; a Restek Rtx-5MS capillary column (5% diphenyl-95% dimethylpolysiloxane, 30 m x 0.25 mm, 0.25 μm) and a Perkin-Elmer Turbo Mass Goldmass-spectrometer. The oven temperature was programmed to run at 60 °C for 5 min and then to increase by 15 °C min^{-1} to a final temperature of 280 °C. A NIST mass spectral library version 1.7 was used for peak identification. The quantitative determination of DCM was performed elaborating its corresponding calibration curve in the 0.0125 and 0.15 mol L^{-1} range.

2.3.2 Study of the effect of pH, time and concentration of MCPA

To evaluate the effect of pH, MCPA sorption experiments were carried out at solid/liquid ratio of 0.5 g L^{-1} obtained by adding 5 mg of NTs to a final volume of 10 mL, using a fixed pesticide concentration of 10 μmol L^{-1}, obtained by diluting 1000 μmol L^{-1} stock solution, varying the pH from 3.0 to 9.5 and for an incubation time of 24 h. The pH was controlled by addition of 0.01 mmol L^{-1} HCl or NaOH to the solution. After incubation in a rotatory shaker at 20 °C, the samples were centrifuged at 7000 rpm for 20 min. The amount of adsorbed MCPA was calculated as the difference between the MCPA quantity initially added and that present in the liquid at equilibrium. Blanks of MCPA in ultrapure water were analyzed in order to check for pesticide stability and/or sorption on the vials.

To evaluate the effect of time on MCPA adsorption, experiments were performed at solid/liquid ratio of 0.5 g L^{-1} using 7.0 μmol L^{-1} of MCPA at pH 3.5. The suspensions were stirred

225 for 2.0, 5.0, 10, 20, 40, 60, 90, 120, 300, 1080, 1440, 1680 and 2880 min. Different volumes of a
226 stock solution of herbicide (1000 μmol L^{-1}) were added to the NTs containing liquid to have initial
227 MCPA concentration in the 0.05 - 260 μmol L^{-1} range. The pH was kept constant at 3.5 by addition
228 of 0.10 or 0.01 mol L^{-1} HCl or NaOH. The samples were incubated for 1440 min and, then, after
229 centrifugation, the supernatants were analyzed as described above.

230 During desorption experiments, immediately after adsorption of 255 and 170 μmol L^{-1} initial
231 MCPA concentration, the samples were put in contact with different volumes of ultrapure water, so
232 to determine the amount of released herbicide. In particular, 10 mL of supernatant was removed and
233 replaced with 10 mL of ultrapure water. After shaking at 25 °C for 24 h, the suspensions were
234 centrifuged and the concentration of released herbicide in the supernatant was determined. The
235 same procedure was repeated by replacing 3.0, 4.0, and 6.0 mL of supernatant with the same
236 volume of ultrapure water.

237

238 *2.3.3 Study of the effect of pH, time and concentration of DCM*

239 In order to study the effect of pH, sorption experiments were made at a solid/liquid ratio of
240 0.5 g L^{-1} obtained by adding 5 mg solid to a final volume of 10 mL, using a constant DCM
241 concentration of 0.15 mol L^{-1}, varying the pH from 3.5 to 7.0 and with an incubation time of 24 h.
242 pH was controlled by addition of 0.01 mmol L^{-1} HCl or NaOH. After incubation in a rotatory shaker
243 at 20 °C, the samples were centrifuged at 7000 rpm for 20 min. The amount of adsorbed DCM was
244 calculated as the difference between the initially added quantity of DCM and the quantity present at
245 equilibrium in the liquid. Blanks of DCM in ultrapure water were analysed in order to check for
246 pollutant stability and sorption on the vials.

247 In order to study the effect of time, experiments were performed at a solid/liquid ratio of 0.5
248 g L^{-1} by using 0.15 mol L^{-1} of DCM at pH 5.5. The suspensions were stirred for 2.0, 5.0, 10, 20, 40,
249 60, 90, 120, 300, 1080, 1440, 1680 and 2880 min.

The adsorption isotherm was obtained as follows: different volumes of a stock solution of DCM (0.15 mol L^{-1}) were added to the Me-IMO NTs containing liquid in such a way to have an initial DCM concentration in the 0.0125 - 0.15 mol L^{-1} range. The pH of each suspension was kept constant at 5.5 by adding 0.10 or 0.01 mol L^{-1} HCl or NaOH. The samples were incubated for 300 min and, then, after centrifugation, the supernatants were analysed as described above.

During desorption experiments, the sample obtained immediately after adsorption from 0.15 mol L^{-1} DCM initial concentration, was put in contact with different volumes of ultrapure water at standard pH value, so to determine the amount of released DCM. In particular, 10 mL of supernatant was removed and replaced by 10 mL of ultrapure water. After shaking at 25 °C for 5 h, the suspension was centrifuged and the concentration of released DCM was determined. The same procedure was made by replacing 3.0, 4.0, and 6 mL of supernatant with the same volume of ultrapure water.

3. Results and discussion

3.1. Relevant physico-chemical features of the Me-IMO NTs in powder and water suspension.

Figure 1 reports the powder XRD pattern (a), the N_2 adsorption/desorption isotherm at -196 °C (b), the PSD and cumulative volume (c) and the ζ-potential curve (d) of the Me-IMO NTs. In Fig. 1a, the main reflection at 3.32 2θ and the halo at 8.84 2θ degrees are characteristic of NTs organized into a pseudo-hexagonal arrangement (Bursill et al., 2000; Bottero et al., 2011). The value of the cell parameter (Table 2) was a = 3.02 nm, as calculated by applying the equation $a = \frac{2}{\sqrt{3}} d_{100}$: the cell parameter is larger than that of IMO NTs (Cradwick et al., 1972), due to larger A pores (*vide infra*).

Fig. 1b shows a type IV N_2 isotherm, with a limited (type H4) hysteresis loop. The steep increase of the adsorbed volume at low P/P^0 values indicates occurrence of some micropores,

275 whereas the rounded knee below 0.1 P/P^0 is due to the presence of very narrow mesopores. The
276 corresponding values of BET SSA and pore volume (Table 2) are typical of Me-IMO NTs (Bottero
277 et al., 2011). Accordingly, the PSD curve (circles in Fig. 1c) shows the occurrence of (mainly)
278 narrow mesopores with an average diameter of *ca.* 2.0 nm (A pores). The value of micropore
279 volume that can be extrapolated from the cumulative pore volume curve (squares in Fig. 1c) is close
280 to that reported in Table 2, which is obtained by the *t*-plot method (0.085 $cm^3\ g^{-1}$).

281 The ζ-potential curve (Fig. 1d) shows that the NTs are positively charged in a broad pH
282 range, and have a point of zero charge equal to 8.6. Nonetheless, the lines at $\zeta = \pm 37$ mV show
283 range of ζ potential reported in the literature for stable suspensions (Honary and Zahir, 2013),
284 indicating that above pH = 5 some NTs aggregation may occur. Such a phenomenon could affect
285 the adsorption/desorption experiments (*vide infra*).
286

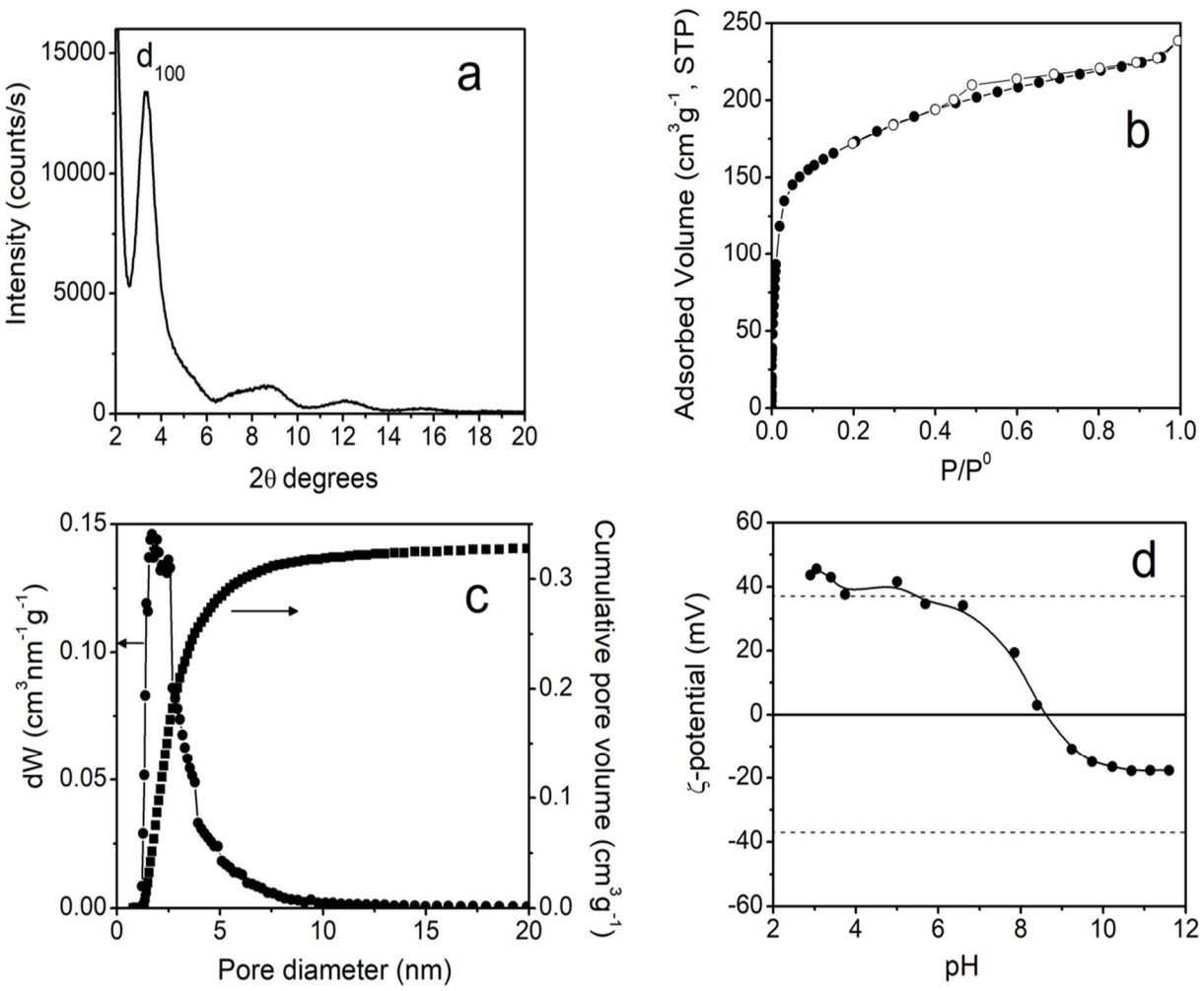


Figure 1. Section a: low angle XRD pattern of Me-IMO powder; section b: N_2 isotherm at -196 °C (black symbols: adsorption branch; white symbols: desorption branch); section c: NL-DFT PSD (circles) and cumulative pore volume (squares) as obtained by applying a N_2 - silica kernel to the isotherm adsorption branch; section d: ζ-potential curve of Me-IMO NTs as a function of pH.

Table 2. Some textural properties of Me-IMO NTs as obtained by N_2 isotherms at -196 °C, X-ray powder diffraction and SAXS experiments with either the dry powder or the water dispersed one.

Sample	BET SSA ($m^2\ g^{-1}$)	Total Pore Volume ($cm^3\ g^{-1}$)	*t*-plot Micropore Volume ($cm^3\ g^{-1}$)	Cell parameter *a* (nm) XRD	Inner radius (nm) (SAXS)	Wall thickness (nm) SAXS
Me-IMO	615	0.35	0.085	3.02	0.91 (0.92[a])	0.55

						(0.56[a])

[a] Value for Me-IMO NTs re-suspended in water.

Figure 2a compares the SAXS spectra of the Me-IMO NTs powder under vacuum and of the same re-dispersed in water (NTs concentration = 5 g L^{-1}): the two patterns are very close, indicating that re-dispersion in water does not induce significant changes in the NTs shape. Only small variations at small angles indicate that the NTs bundling may be slightly affected by re-dispersion in water, with a consequent decrease of the average bundle size. The internal contrast is also modified.

Fig. 2b compares the experimental SAXS pattern of Me-IMO NTs powder dispersed in water (NTs concentration = 5 g L^{-1}) with the calculated patterns for isolated NTs and for NTs in small bundles. In agreement with the powder XRD pattern, comparison of the SAXS curves clearly indicates the presence of bundles when the powder is re-dispersed in water. The NTs inner radius, as obtained by SAXS, is r_i = 0.91 nm and the wall thickness is t_w = 0.55 nm. The experimental peak position in SAXS at q = 0.238 A^{-1} cannot be directly associated to the hexagonal lattice parameter due to the peak shift induced by the NTs form factor. The lattice parameter that is obtained by the computed SAXS pattern is 3.05 nm, i.e. a value that well corresponds to the NTs external diameter, with a small additional separation of 0.15 nm.

The geometric values obtained from XRD and SAXS are in very good agreement with the pores diameter as measured by N_2 isotherm. Indeed, according to the determined sizes, the micropore volume is 0.095 cm^3 g^{-1}, in fair agreement with the value as determined by the *t*-plot method (0.085 cm^3 g^{-1}). The small difference may be due to tiny amounts of water or anions trapped within the B pores, which occupy a small part of the volume, finally explaining the 0.15 nm additional distance in the bundle lattice parameter.

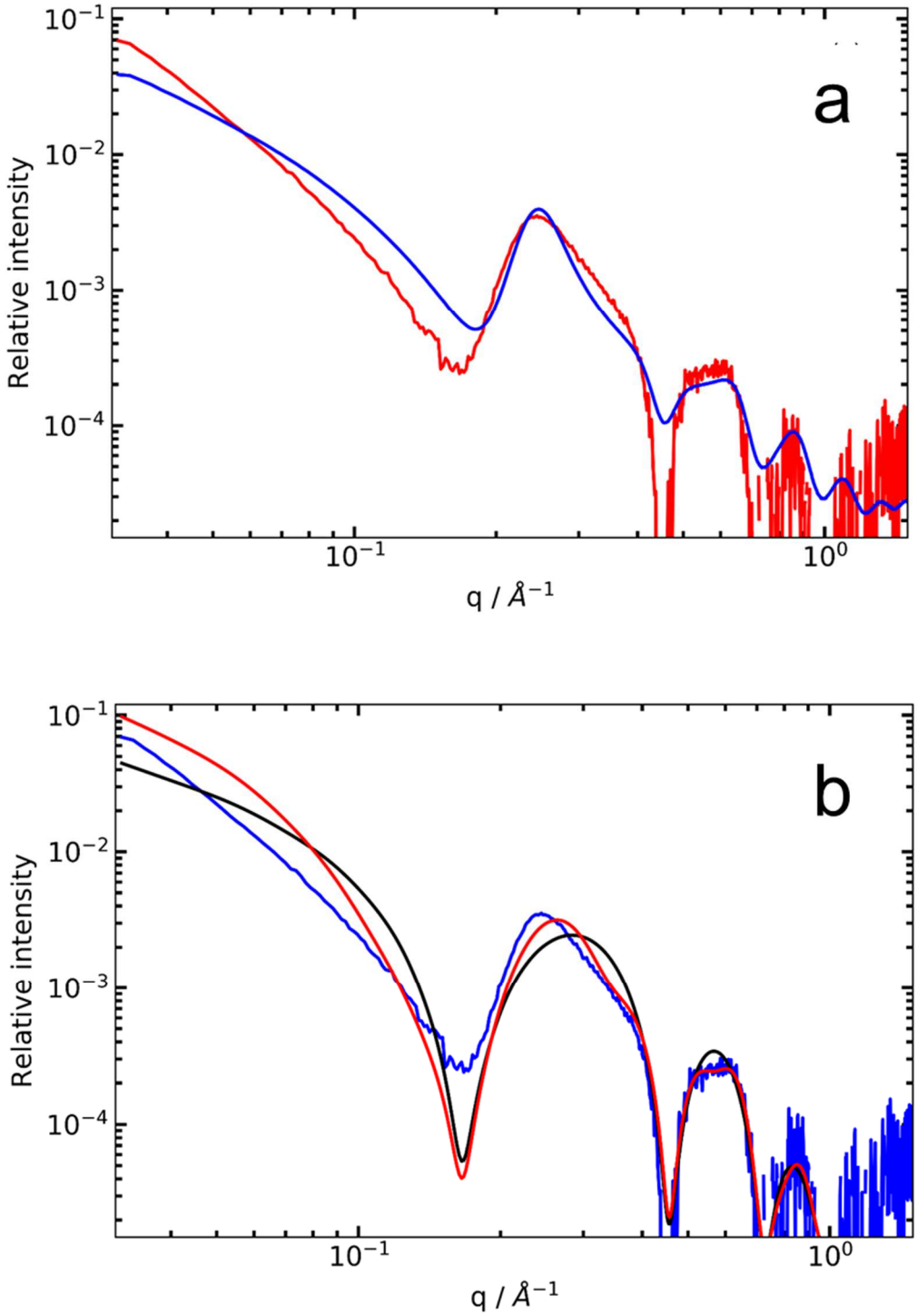


Figure 2. Section a: SAXS patterns of Me-IMO NTs as dry powder (blue curve) and re-dispersed in water (5 g L^{-1}, red curve). Section b: SAXS pattern of NTs in water (blue curve) compared to a scattering model of dispersed hollow NTs (with r_i = 0.91 nm, wall thickness = 0.55 nm, internal electronic density = 0.05 $e^-/Å^3$, black curve) and to a scattering model considering bundles (red curve).

The SAXS analysis also allowed obtaining the inner and outer electron density (ρ_i and ρ_e) of the NTs in both the dry powder and after re-dispersion in water. Interestingly, ρ_i is equal to 0.05 $e^-/Å^3$ in both samples. As compared to the electron density of bulk water (ρ_{H2O} = 0.334 $e^-/Å^3$), such a low inner density means that in the powder (which was treated under vacuum at r.t. and not outgassed at high temperature) only few H_2O molecules occur within the NTs and that the powder is extremely hydrophobic, as ρ_i did not increase upon contact with water.

3.2. Adsorption of MCPA as studied in batch conditions and by SAXS

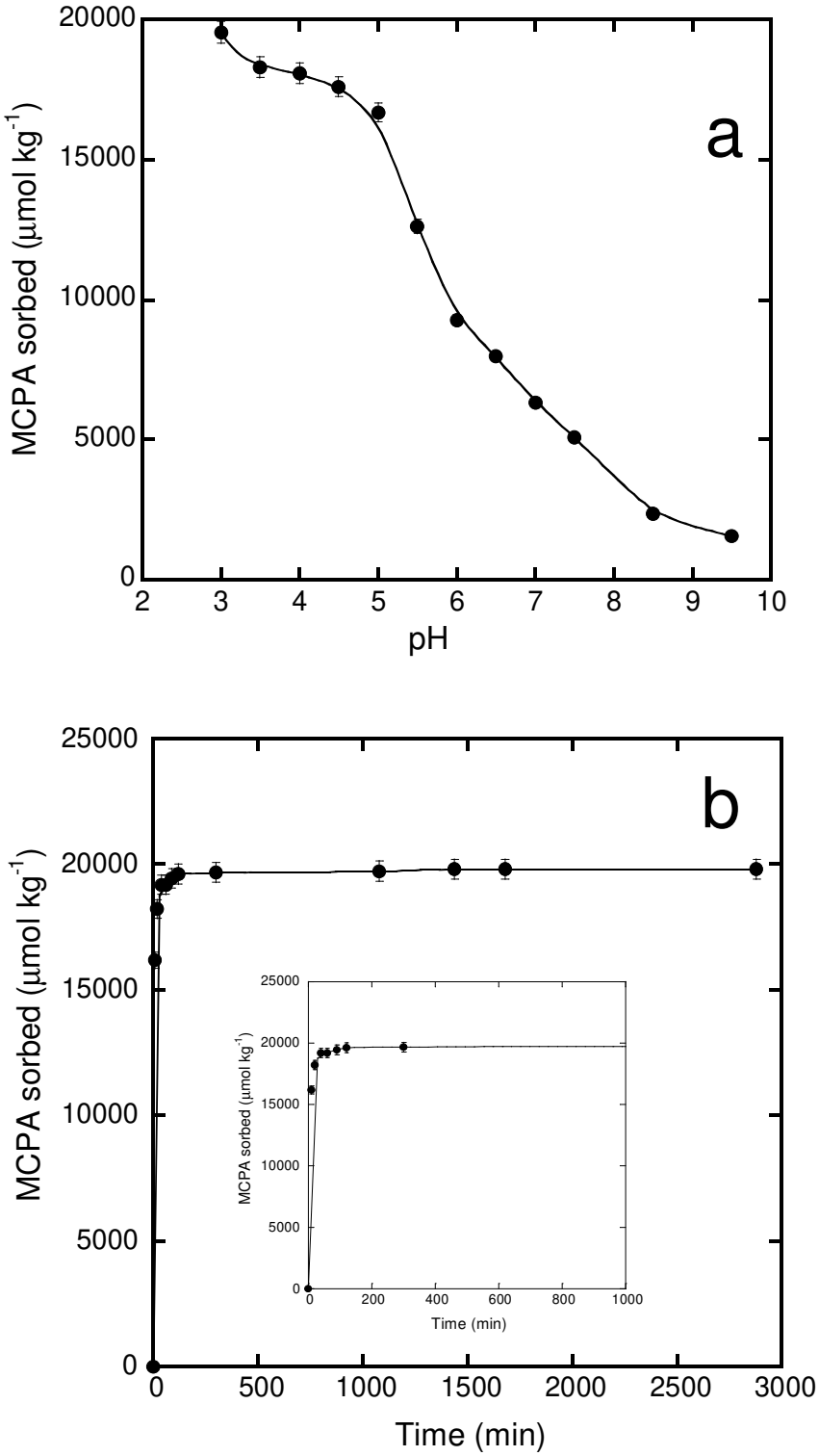
Fig. 3a shows the adsorbed amount of MCPA (μmol kg^{-1}) as a function of pH (each point having being acquired after 24 h incubation): as a whole, the overall amount of adsorbed MPCA is maximum below pH 4, decreasing as pH increases. Such a behaviour may be interpreted by considering the ζ-potential curve in Fig. 1d, where the net positive charge of the NTs progressively decreases as pH increases, until the PZC is reached (pH 8.6). In agreement with SAXS data in Fig. 5 (*vide infra*), the curve in Fig. 3a seems to point out the fact that the herbicide mainly interacts with the NTs outer surface.

Fig. 3b shows the adsorbed amount of MCPA as a function of time at a constant pH of 3.5, i.e. a pH value at which simultaneously the adsorbed amount is very high (Fig. 3a) and the NTs ζ potential is ca.+ 37 mV, a condition proper of a stable suspension (Honary and Zahir, 2013). In such condition, aggregation of NTs into bundles should be limited, finally maximizing the available external surface and, thus, MCPA adsorption. The curve in Fig. 3b shows indeed a steep increase in the adsorbed MCPA during the first minutes (inset), reaching complete adsorption after 1440 min. In the adopted experimental conditions (i.e. pH = 3.5 and initial concentration of MCPA = $1.0*10^{-5}$ M), such a phenomenon can be readily assigned to the occurrence of electrostatic interactions. The

best model describing the sorption kinetics in Fig. 3b was the pseudo second-order model, which can be expressed in a linear form according to eq. (2) (Ozacar and Sengyl, 2006):

$$\frac{t}{q} = \frac{1}{k_2 * q_e^2} - \frac{t}{q_e} \qquad (2)$$

where q_e and q are the amount of organic pollutant adsorbed (µmol kg^{-1} MCPA) at equilibrium and at time *t*, respectively, k_2 is the rate constant of adsorption (kg/µmol h) and *t* is the time (h). For MCPA, the following values where calculated q_e = 19821.99 µmol kg^{-1} and k_2 = 1.558 x 10^{-3} kg/µmol h, with an r^2 = 1 confirming that the curve-fit procedure was appropriate.



358

359 **Figure 3**. Section a: MCPA adsorbed amount as a function of pH (incubation time = 24 h;

360 initial MCPA concentration = $1.0*10^{-5}$ M). Section b: MCPA adsorbed amount as a function of time

361 at pH = 3.5 (initial MCPA concentration = $1.0*10^{-5}$ M). Inset to section b: magnification of the 0-
362 1000 min range.

363 Figure 4 reports MCPA adsorption/desorption equilibrium isotherms at pH = 3.5. The
364 adsorption isotherm (black symbols) has a complex shape, which can be due to multiple phenomena
365 occurring at the NTs outer surface at increasing MCPA concentration. Being the pKa of MCPA in
366 water equal to 2.90 (Addorisio et al., 2010), at pH = 3.5 its dissociation degree (α) is ca. 0.5 and,
367 thus, besides electrostatic interaction, other types of interactions may occur with the outer surface of
368 NTs, like H-bonding, as previously shown by some of us for MCPA adsorption on (mesoporous)
369 Al_2O_3 and Fe_2O_3. (Addorisio et al., 2010) Interestingly, at higher MCPA equilibrium concentration,
370 the adsorption isotherm becomes convex, indicating that the adsorbing species has a lower affinity
371 for the adsorbent: multi-layer adsorption could, indeed, occur, as in MCPA crystals, where multiple
372 inter-molecular bonds form (Kobyłecka et al., 2015).

373 So far, different adsorbents have been investigated for the removal of phenoxy herbicides,
374 including layered double hydroxides (Bruna et al., 2009; Ahmad et al., 2010; Kamaraj et al., 2014),
375 mesoporous metal oxides (Addorisio et al., 2010), resins (Ding et al., 2012) and carbon materials
376 (Kim et al., 2008). In particular, MCPA adsorption was studied on an Argentine montmorillonite
377 (MMT) and its organo-hybrid (OMMT) (Santiago et al., 2016): although adsorption on OMMT
378 (0.05 mol/kg) increased with respect to MMT (*ca.* 0.01 mol/kg), the MCPA adsorbed amounts were
379 significantly lower with respect to that obtained in the adopted experimental conditions with Me-
380 IMO NTs, i.e. *ca.* 0.2 mol/kg. Such a value is particularly sound if compared to the amount of
381 MCPA adsorbed at pH = 4.0 on a mesoporous alumina with SSA = 195 $m^2 g^{-1}$ (0.01 mol/kg), i.e. an
382 adsorbent with similar chemical composition, where diffusion limits occurred (Addorisio et al.,
383 2010).

384 Here, MCPA adsorption likely occurs at the outer surface of the NTs, thus overcoming the
385 aforementioned diffusion limitations during adsorption. However, the two desorption curves (white
386 symbols, Fig. 4) showed that, in the adopted experimental conditions, MCPA adsorption is only

partially irreversible, in that the desorbed amount of MCPA was ca. the 35 % and the 44% of the total amount of adsorbed MCPA (when starting from 129820 μmol/kg and 84790 μmol/kg. respectively). It should be noticed that MCPA adsorption at the outer surface of the NTs is surely perturbing their actual surface charge, which very likely decreases and, thus, the dispersion could become less stable, with consequent NTs agglomeration, finally hampering effective desorption of MCPA.

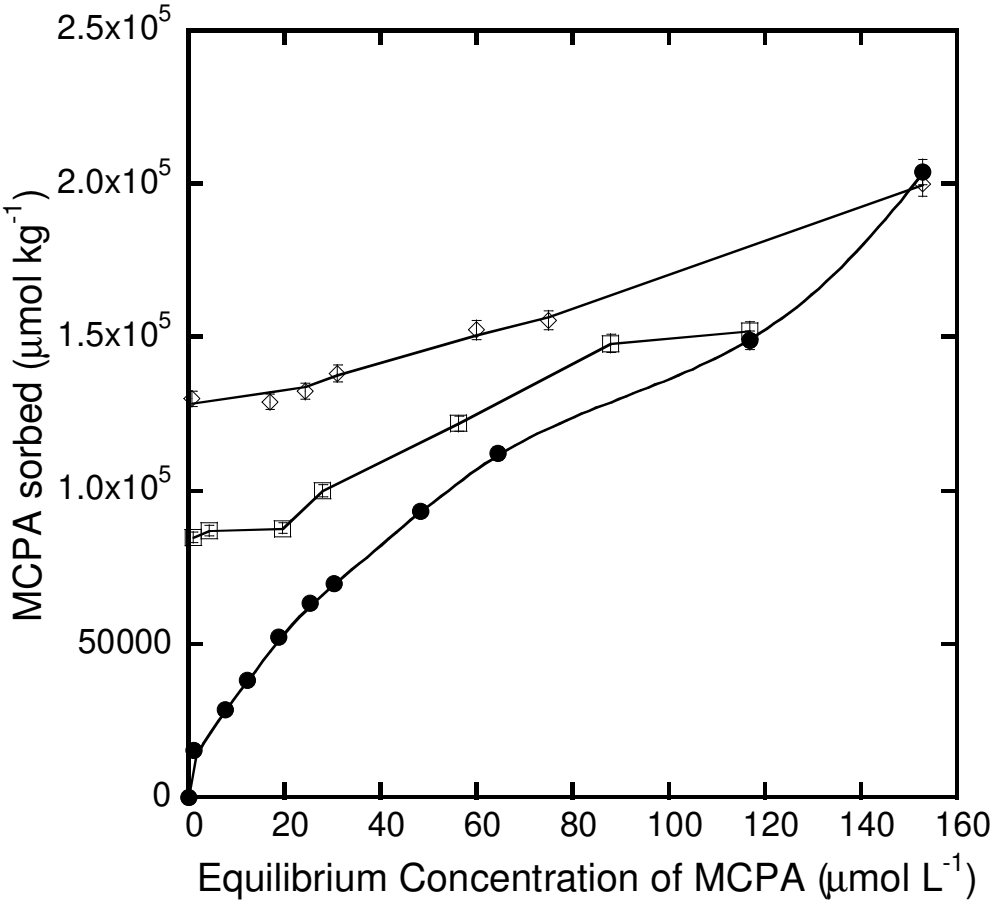


Figure 4. Adsorption (black circles) isotherm and desorption (white symbols) isotherms of MCPA on Me-IMO-NTs as obtained at pH = 3.5 in the 0 -160 μmol L^{-1} equilibrium concentration range.

In order to confirm the preferential interaction with the outer surface of NTs, Figure 5a reports the SAXS spectra taken after contacting the Me-IMO NTs with MCPA $1.0*10^{-4}$ M in water

at pH 3.7, 4.5, 9.6 and 10.4. The bulk electron density of MCPA is ρ_{MCPA} = 0.48 $e^-/Å^3$. In principle, the molecular size of MCPA (Table 1) allows adsorption within A pores: if so, a corresponding increase of the NTs inner electronic density should be measured by SAXS (Fig. 5), since the position of the first minimum of the scattered intensity is very sensitive to changes of the internal scattering length density. In order to better illustrate this, the scattered intensities of model NTs with internal electronic density varying from 0.05 to 0.2 e/A^3 are plotted in Fig. 5. Interestingly, the position of the first minimum of the experimental scattered intensity does not shift with pH. Such a constant inner NTs electronic density allows excluding any interaction of MCPA with the NTs inner surface.

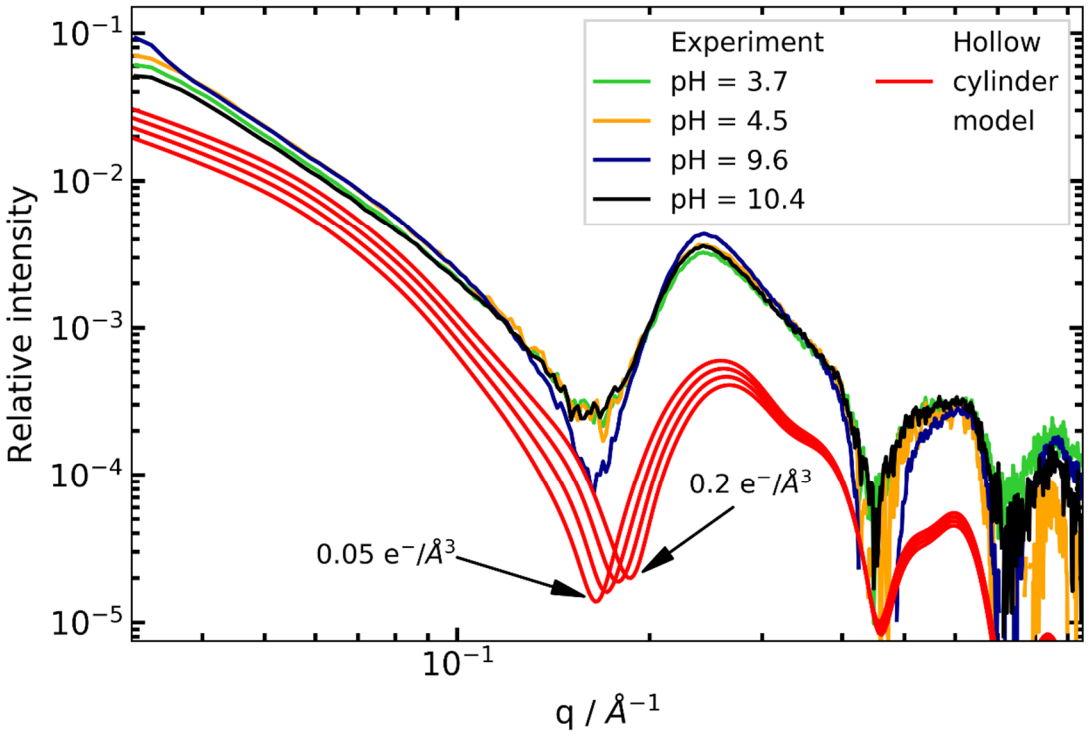


Figure 5. Experimental SAXS patterns of Me-IMO NTs in MCPA water suspensions at pH = 3.7, 4.5, 9.6 and 10.4 and calculated SAXS patterns (red curves), showing a shift of the scattering model of hollow cylinder at increasing internal electronic density (from 0.05 to 0.2 $e^-/Å^3$).

3.3. Adsorption of DCM as studied in batch conditions and by SAXS.

Figure 6a reports the pH dependence of DCM adsorbed on Me-IMO NTs: the curve shape is very different with respect to that concerning MCPA (Fig. 3a), where the adsorbed amount decreases with pH because, simultaneously, the NTs outer surface becomes less positively charged. With DCM, adsorption is maximum at pH = 5.5 and, then, decreases.

DCM has a non-negligible dipole moment (μ = 1.470 D) and can be polarized by the polar outer NTs walls, leading to dipolar interactions. Simultaneously, its kinetic diameter (0.33 nm) allows DCM diffusion within A pores, but also within B pores having a diameter of 0.45 nm, (Bottero et al., 2011; Bonelli et al., 2013b) and which are able to strongly polarize $CO_{2(g)}$ molecules in gas-solid systems (Zanzottera et al., 2012a; Bonelli et al., 2013b). Although different phenomena affect adsorption in liquid/solid systems, it is interesting to notice that DCM adsorption is maximum at pH 5.5, at which the ζ-potential of the Me-IMO NTs is ca. + 30 mV, likely implying some NTs agglomeration with formation of (more) B pores, where the DCM molecules may diffuse and be polarized, like $CO_{2(g)}$ molecules (Zanzottera et al., 2012a). Accordingly, the kinetic curve in Fig. 6b has a smooth knee (inset) before reaching a plateau, indicating that more than one type of interaction likely occurs. Application of eq. (2) to model the DCM sorption kinetics in Fig. 6b (Ozacar and Sengyl, 2006) allowed calculating the following parameters: q_e = 209.04 mol kg^{-1} and k_2 = 0.0305 kg/mol h, r^2 = 0.99. The extremely high amount of adsorbed DCM could be explained by considering that in oil/water emulsions, such hybrid NTs adsorb at the oil/water interface, stabilizing Pickering emulsions (Picot et al., 2016), modifying the viscosity and, possibly, favouring transport of small molecules within the NTs.

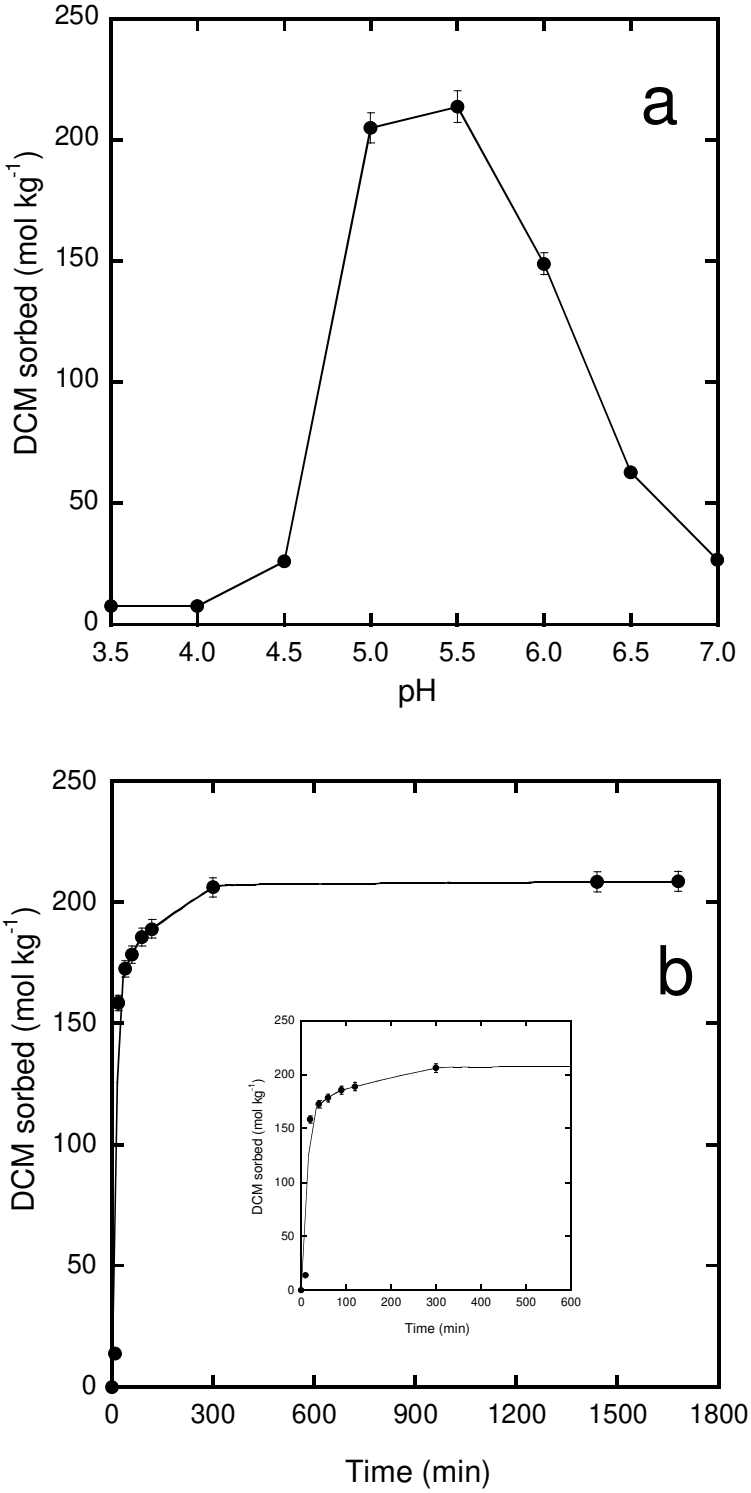
Accordingly, the adsorption isotherm in Fig. 7 (black symbols) has an S-shape, indicating that at least two types of adsorption phenomena occur: at low concentration, DCM molecules should interact with stronger adsorbing sites, since their sizeable dipole moment allows interaction with polarizing sites, like B pores, stemming from partial NTs agglomeration into small bundles, and able to polarize DCM molecules (kinetic diameter = 0.33 nm). At increasing pH value, the outer surface of NTs (C surface) becomes less positively charged, thus lowering the adsorption

capacity of the outer surface of the NTs towards DCM molecules. Unfortunately, the electronic density of DCM (Table 1) is very close to that of water (ρ_{H2O} = 0.334 $e^-/Å^3$) and, thus, if such a phenomenon should happen, it would be hardly discernible by SAXS, which instead could readily show DCM diffusion within the NTs (A pores, *vide infra*). The latter phenomenon is likely responsible of the largest adsorbed amount of DCM above 0.02 mol/L equilibrium concentration, although in those conditions an oil-in-water Pickering emulsion could form (Picot et al., 2016).

As a whole, the thorough understanding of the interaction of DCM with Me-IMO NTs is complicated both by the nature of the pollutant and by formation of Pickering emulsions (Picot et al., 2016).

Concerning DCM removal from polluted water, adsorption is considered by the literature as one the most applicable techniques (Lemus et al., 2012; Zhou et al., 2014, 2017), but it requires porous materials with sound adsorbing capacity and high stability. The DCM adsorption capacity of Zr-based metal-organic framework (UiO-66) was enhanced in the presence of UiO-66 crystals with various morphologies and optimized porous structure as obtained by adjusting the synthesis procedure.(Zhou et al., 2017): however, in the adopted experimental conditions, the maximum adsorption capacity was lower than here (ca. 6 mmol/kg).

As for MCPA, in the adopted experimental conditions DCM desorption was not fully reversible (white symbols in Fig. 7) indicating the likely occurrence of mass transfer phenomena, related to some NTs aggregation, which hampers DCM molecules diffusion of DCM from the interior of the NTs/bundles to the exterior. However, such diffusion limitations, occurring especially during desorption, could be overcome by changing operative conditions, e.g. liquid/solid ratio, and require dedicated studies.



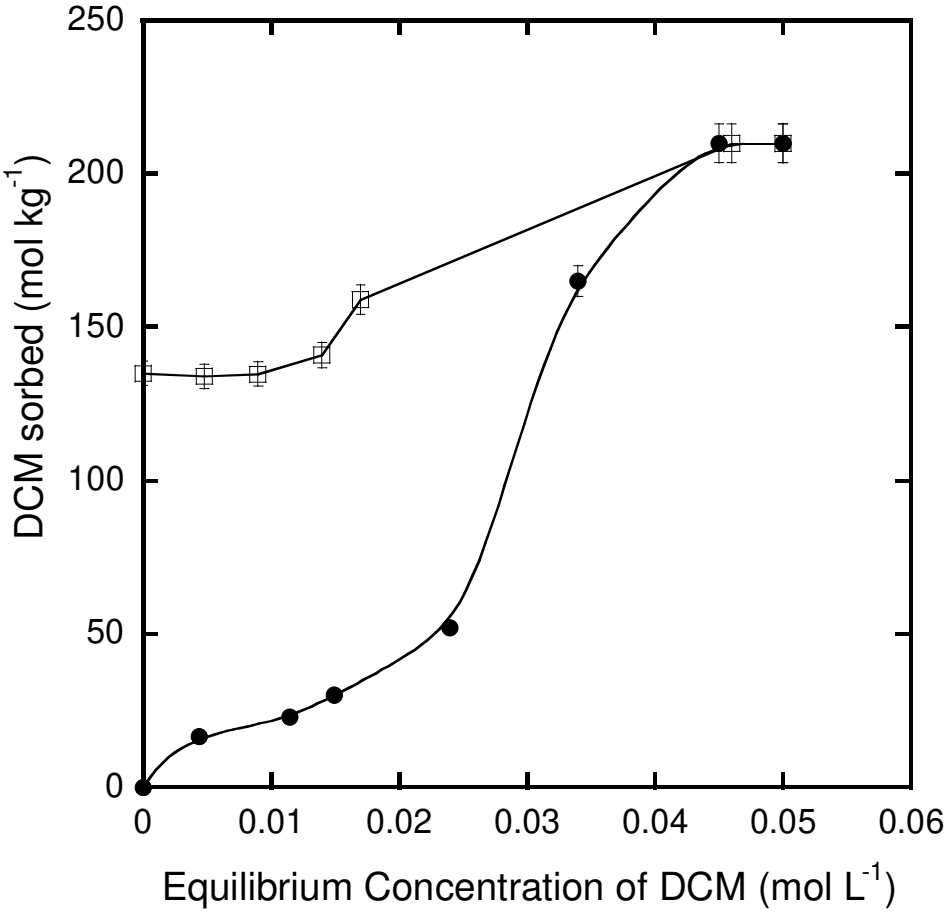
462

463

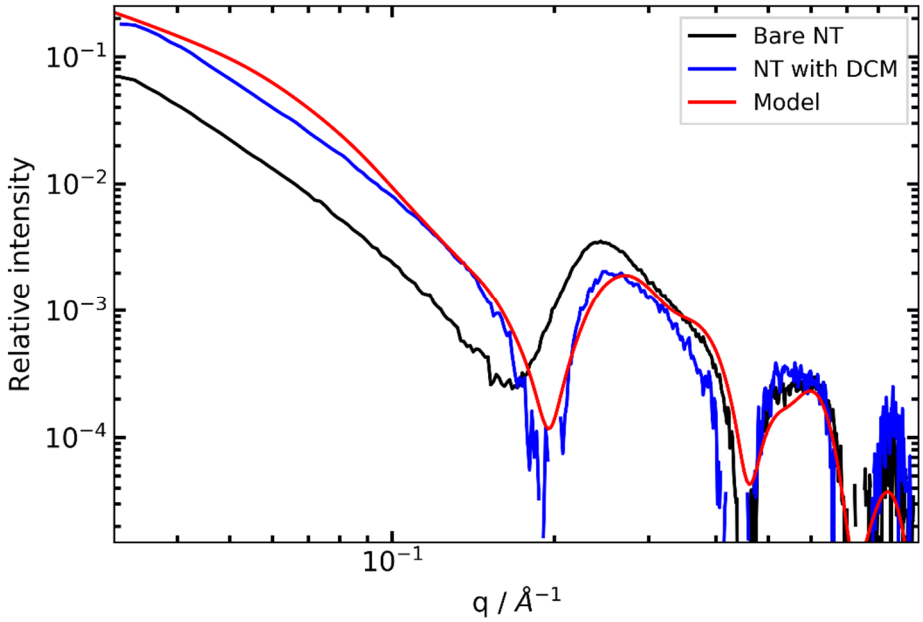
464 **Figure 6.** Section a: DCM adsorbed amount as a function of pH. Incubation time: 24 h.

465 Initial DCM concentration: 0.15 M. Section b: DCM adsorbed amount as a function of time. pH =

466 5.5; initial DCM concentration: 0.15 M. Inset to section b: magnification of the 0-600 min range,
467 where the maximum amount of adsorbed DCM is reached after 300 min.
468



469
470
471 **Figure 7.** Adsorption (black symbols) isotherm and desorption isotherm (white symbols) of DCM
472 on Me-IMO-NTs at pH = 5.5 in the 0 -0.06 mol L^{-1} equilibrium concentration range.
473



474

475 **Figure 8.** SAXS patterns of Me-IMO NTs in the DCM suspension at natural pH. The scattering
476 model for a hollow cylinder show the variation of internal electronic density from 0.05 to 0.29 e^-
477 /$Å^3$.

478

479 Fig. 8 reports the SAXS patterns observed when the NTs are contacted with DCM
480 suspension. The position of the first minimum shifts towards higher q values, indicating an increase
481 of the inner electronic density. The applied model yields a value of ρ_i equal to 0.29 e/$Å^3$ for the
482 inner electron density of Me-IMO NTs, proving that DCM (bulk DCM has $\rho = 0.4$ e/$Å^3$, Table 1)
483 has indeed entered the NTs. The high adsorbed amounts measured by batch experiments indicate
484 that the DCM molecules adsorb also at the outer surface of NTs and not only within them, but since
485 the SAXS measurement is based on a change on the internal electron density, it may be unable to
486 detected the change in the outer electron density, since the NTs are suspended in water, which has a
487 high electron density.

488

489 **Conclusions**

490 Methylimogolite NTs have two types of surface, namely an inner one, which is extremely
491 hydrophobic, and an outer one, which is hydrophilic, polar and positively charged below pH 8.6.
492 The external positive charge affects the NTs behaviour in water: for instance, by varying pH, NTs
493 arrangement changes, likely leading to some aggregation phenomena that, in turn, affect both
494 adsorption and desorption processes in water.

495 Adsorption of two organic pollutants (namely MCPA, 2-methyl-4-chlorophenoxyacetic acid,
496 and DCM, dichloromethane) on methylimogolite occurs through complex interactions, which can
497 be only partially explained by the joint use of batch experiments and SAXS measurements.

498 On the one hand, the reported results show that MCPA adsorption occurs at the outer surface
499 of the NTs by means of both electrostatic interactions and intermolecular forces, with sound overall
500 adsorbed amounts as compared to another mesoporous adsorbent (i.e. Al_2O_3) with a chemical
501 composition similar to that of the NTs outer surface.

502 On the other hand, unravelling the type of interaction of DCM with methylimogolite is not
503 straightforward. SAXS measurements clearly showed diffusion of DCM molecules within A pores
504 and batch experiments showed high adsorbed amounts. However, the latter type of measurements
505 seem to point out the interaction with another type of surface, most likely B pores forming among
506 three aligned NTs in a bundle: unfortunately, this type of interaction that cannot be clearly assessed
507 by SAXS. Moreover, on the basis of previous studies, stabilization of an emulsion induced by the
508 same NTs could not be excluded.

509 To the best of our knowledge, this is the first work assessing the adsorption/desorption of
510 organic molecules of environmental concern with this type of nanomaterial and could open new
511 perspectives for its practical application, undoubtedly after optimization of the desorption process,
512 which requires dedicated studies.

513

Acknowledgements

Financial support from Università Italo-Francese (Galileo Project Grant n°G16 – 34 «Hybrid imogolite nanotubes for environmental applications») is acknowledged.

References

Ackerman, W.C., Smith, D.M., Huling, J.C., Kim, Y.W., Bailey, J.K., Brinker, C.J., 1993. Gas/Vapor Adsorption in Imogolite: A Microporous Tubular Aluminosilicate. Langmuir 9, 1051–1057. https://doi.org/10.1021/la00028a029

Addorisio, V., Esposito, S., Sannino, F., 2010. Sorption Capacity of Mesoporous Metal Oxides for the Removal of MCPA from Polluted Waters. J. Agric. Food Chem. 58, 5011–5016. https://doi.org/10.1021/jf9044815

Ahmad, T., Rafatullah, M., Ghazali, A., Sulaiman, O., Hashim, R., Ahmad, A., 2010. Removal of pesticides from water and wastewater by different adsorbents: A review. J. Environ. Sci. Heal. - Part C Environ. Carcinog. Ecotoxicol. Rev. 28, 231–271. https://doi.org/10.1080/10590501.2010.525782

Amara, M.S., Paineau, E., Tache, O., Launois, P., Thill, A., 2015. Hybrid , Tunable-Diameter , Metal Oxide Nanotubes for Trapping of Organic Molecules. https://doi.org/10.1021/cm503428q

Bahadori, E., Vaiano, V., Esposito, S., Armandi, M., Sannino, D., Bonelli, B., 2018. Photo-activated degradation of tartrazine by H_2O_2 as catalyzed by both bare and Fe-doped methyl-imogolite nanotubes. Catal. Today 304, 199–207. https://doi.org/10.1016/j.cattod.2017.08.003

Bonelli, B., 2016. Surface Chemical Modifications of Imogolite, in: Yuan, P., Thill, A., Bergaya, F. (Eds.), Developments in Clay Science. Elsevier B.V, pp. 279–307. https://doi.org/10.1016/B978-0-08-100293-3.00012-1

538 Bonelli, B., Armandi, M., Garrone, E., 2013a. Surface properties of alumino-silicate single-walled
539 nanotubes of the imogolite type. Phys. Chem. Chem. Phys. 15, 13381–13390.
540 https://doi.org/10.1039/c3cp51508g

541 Bonelli, B., Bottero, I., Ballarini, N., Passeri, S., Cavani, F., Garrone, E., 2009. IR spectroscopic
542 and catalytic characterization of the acidity of imogolite-based systems. J. Catal. 264, 15–30.
543 https://doi.org/10.1016/j.jcat.2009.03.003

544 Bonelli, B., Zanzottera, C., Armandi, M., Esposito, S., Garrone, E., 2013b. IR spectroscopic study
545 of the acidic properties of alumino-silicate single-walled nanotubes of the imogolite type.
546 Catal. Today 218–219, 3–9. https://doi.org/10.1016/j.cattod.2013.02.004

547 Bottero, I., Bonelli, B., Ashbrook, S.E., Wright, P.A., Zhou, W., Tagliabue, M., Armandi, M.,
548 Garrone, E., 2011. Synthesis and characterization of hybrid organic/inorganic nanotubes of the
549 imogolite type and their behaviour towards methane adsorption. Phys. Chem. Chem. Phys. 13,
550 744–750. https://doi.org/10.1039/c0cp00438c

551 Boyer, M., Paineau, E., Bacia-verloop, M., Thill, A., 2014. Applied Clay Science Aqueous
552 dispersion state of amphiphilic hybrid aluminosilicate nanotubes. Appl. Clay Sci. 96, 45–49.
553 https://doi.org/10.1016/j.clay.2014.04.022

554 Bruna, F., Celis, R., Pavlovic, I., Barriga, C., Cornejo, J., Ulibarri, M.A., 2009. Layered double
555 hydroxides as adsorbents and carriers of the herbicide (4-chloro-2-methylphenoxy)acetic acid
556 (MCPA): Systems Mg-Al, Mg-Fe and Mg-Al-Fe. J. Hazard. Mater. 168, 1476–1481.
557 https://doi.org/10.1016/j.jhazmat.2009.03.038

558 Bursill, L.A., Peng, J.L., Bourgeois, L.N., 2000. Imogolite : An aluminosilicate nanotube material.
559 Philos. Mag. A 80, 105–117. https://doi.org/10.1080/01418610008212043

560 Cradwick, P.D.G., Farmer, V.C., Russell, J.D., Masson, C.R., Wada, K., Yoshinaga, N., 1972.

561 Imogolite, a Hydrated Aluminium Silicate of Tubular Structure. Nat. Phys. Sci. 240, 187–189.
562 https://doi.org/10.1038/physci240187a0

563 Ding, L., Lu, X., Deng, H., Zhang, X., 2012. Adsorptive removal of 2,4-dichlorophenoxyacetic acid
564 (2,4-D) from aqueous solutions using MIEX resin. Ind. Eng. Chem. Res. 51, 11226–11235.
565 https://doi.org/10.1021/ie300469h

566 Du, P., Yuan, P., Thill, A., Annabi-Bergaya, F., Liu, D., Wang, S., 2017. Insights into the formation
567 mechanism of imogolite from a full-range observation of its sol-gel growth. Appl. Clay Sci.
568 150, 115–124. https://doi.org/10.1016/j.clay.2017.09.021

569 Freyria, F.S., Geobaldo, F., Bonelli, B., 2018. Nanomaterials for the abatement of pharmaceuticals
570 and personal care products from wastewater. Appl. Sci. 8, 170.
571 https://doi.org/10.3390/app8020170

572 Garrone, E., Bonelli, B., 2016. Imogolite for Catalysis and Adsorption, in: Yuan, P., Thill, A.,
573 Bergaya, F. (Eds.), Developments in Clay Science. Elsevier B.V, pp. 672–707.
574 https://doi.org/10.1016/B978-0-08-100293-3.00025-X

575 Gimeno, O., Plucinski, P., Kolaczkowski, S.T., Rivas, F.J., Alvarez, P.M., 2003. Removal of the
576 Herbicide MCPA by Commercial Activated Carbons : Equilibrium , Kinetics , and
577 Reversibility 22, 1076–1086. https://doi.org/10.1021/ie020424x

578 Gustafsson, J.P., 2001. The surface chemistry of imogolite. Clays Clay Miner. 49, 73–80.

579 Honary, S., Zahir, F., 2013. Effect of Zeta Potential on the Properties of Nano-Drug Delivery
580 Systems - A Review (Part 2) 12, 265–273.

581 Huang, B., Lei, C., Wei, C., Zeng, G., 2014. Chlorinated volatile organic compounds (Cl-VOCs)
582 in environment — sources , potential human health impacts , and current remediation
583 technologies. Environ. Int. 71, 118–138. https://doi.org/10.1016/j.envint.2014.06.013

584 Kamaraj, R., Davidson, D.J., Sozhan, G., Vasudevan, S., 2014. An in situ electrosynthesis of metal
585 hydroxides and their application for adsorption of 4-chloro-2-methylphenoxyacetic acid
586 (MCPA) from aqueous solution. J. Environ. Chem. Eng. 2, 2068–2077.
587 https://doi.org/10.1016/j.jece.2014.08.027

588 Karube, J., 1998. Notes: Hysteris of the colloidal stability of imogolite. Clays Clay Miner. 583–584.
589 https://doi.org/10.1346/CCMN.1998.0460512

590 Kim, T.Y., Park, S.S., Kim, S.J., Cho, S.Y., 2008. Separation characteristics of some phenoxy
591 herbicides from aqueous solution. Adsorption 14, 611–619. https://doi.org/10.1007/s10450-
592 008-9129-6

593 Kobyłecka, J., Turek, A., Siero, L., 2015. Crystal Packing and Supramolecular Motifs in Four
594 Phenoxyalkanoic Acid Crystal Packing and Supramolecular Motifs in Four Phenoxyalkanoic
595 Acid Herbicides — Low-Temperature Redeterminations. Org. Chem. Int. ID 608165.
596 https://doi.org/10.1155/2011/608165

597 Lemus, J., Martin-Martinez, M., Palomar, J., Gomez-Sainero, L., Gilarranz, M.A., Rodriguez, J.J.,
598 2012. Removal of chlorinated organic volatile compounds by gas phase adsorption with
599 activated carbon. Chem. Eng. J. 211–212, 246–254. https://doi.org/10.1016/j.cej.2012.09.021

600 Mackenzie, K.J.D., 1989. Structure and Thermal Transformations of Imogolite Studied by 29Si and
601 27Al High-Resolution Solid-State Nuclear Magnetic Resonance. Clays Clay Miner. 37, 317–
602 324. https://doi.org/10.1346/CCMN.1989.0370404

603 Mizota, C., 1977. Phosphate fixation by ando soils different in their clay mineral composition. Soil
604 Sci. Plant Nutr. 23, 311–318. https://doi.org/10.1080/00380768.1977.10433050

605 Ozacar, M., Sengyl, I., 2006. A two stage batch adsorber design for methylene blue removal to
606 minimize contact time. J. Environ. Manag. 80, 372–379.

https://doi.org/10.1016/j.jenvman.2005.10.004

Parfitt, R.L., 2009. Allophane and imogolite : role in soil biogeochemical processes. Clay Miner. 44, 135–155. https://doi.org/10.1180/claymin.2009.044.1.135

Picot, P., Gobeaux, F., Coradin, T., Thill, A., 2019. Dual internal functionalization of imogolite nanotubes as evidenced by optical properties of Nile red. Appl. Clay Sci. 178, 1015133. https://doi.org/10.1016/j.clay.2019.105133

Picot, P., Malloggi, F., Coradin, T., Thill, A., 2016. Behaviour of hybrid inside/out Janus nanotubes at an oil/water interface. A route to self-assembled nanofluidics? Faraday Discuss. 191, 1–5. https://doi.org/10.1039/C6FD00034G

Poli, E., Elliott, J.D., Hine, N.D.M., Mostofi, A.A., Teobaldi, G., Elliott, J.D., Hine, N.D.M., Mostofi, A.A., Teobaldi, G., Poli, E., Elliott, J.D., Hine, N.D.M., Mostofi, A.A., Teobaldi, G., 2015. Large-scale density functional theory simulation of inorganic nanotubes : a case study on Imogolite nanotubes 19, S272. https://doi.org/10.1179/1432891715Z.0000000001560

Rojas-Mancilla, E., Oyarce, A., Alvarado-soto, L., Ram, R., 2019. Imogolite Synthetized in Presence of As(III) Induces Low Cell Toxicity and Hemolysis , in Vitro , Potential Stabilization of Arsenite Present in Aqueous Systems 4, 10510–10515. https://doi.org/10.1021/acsomega.8b03357

Santiago, C.C., Fernández, M.A., Torres Sánchez, R.M., 2016. Adsorption and characterization of MCPA on DDTMA- and raw-montmorillonite: Surface sites involved. J. Environ. Sci. Heal. - Part B Pestic. Food Contam. Agric. Wastes 51, 245–253. https://doi.org/10.1080/03601234.2015.1120618

Shafia, E., Esposito, S., Armandi, M., Bahadori, E., Garrone, E., Bonelli, B., 2016a. Reactivity of bare and Fe-doped alumino-silicate nanotubes (imogolite) with H_2O_2 and the azo-dye Acid

630 Orange 7. Catal. Today 277, 89–96. https://doi.org/10.1016/j.cattod.2015.10.011

631 Shafia, E., Esposito, S., Bahadori, E., Armandi, M., Manzoli, M., Bonelli, B., 2016b. Synthesis and
632 characterization of Fe-doped aluminosilicate nanotubes with enhanced electron conductive
633 properties. J. Vis. Exp. 117, e54758. https://doi.org/10.3791/54758

634 Thill, A., Picot, P., Belloni, L., 2017. A mechanism for the sphere/tube shape transition of
635 nanoparticles with an imogolite local structure (imogolite and allophane). Appl. Clay Sci. 141,
636 308–315. https://doi.org/10.1016/j.clay.2017.03.011

637 Zanzottera, C., Armandi, M., Esposito, S., Garrone, E., Bonelli, B., 2012a. CO_2 adsorption on
638 aluminosilicate single-walled nanotubes of imogolite type. J. Phys. Chem. C 116, 20417–
639 20425. https://doi.org/10.1021/jp3061637

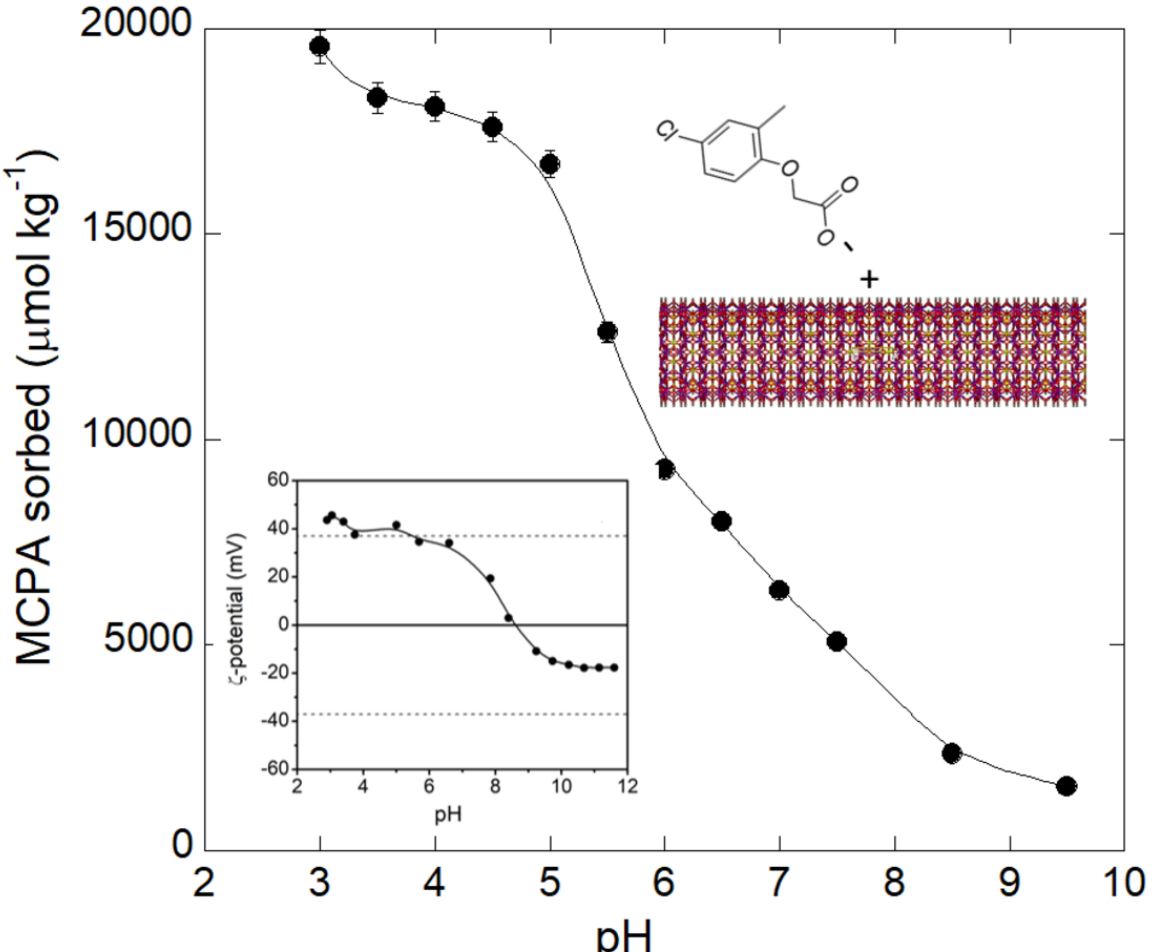
640 Zanzottera, C., Vicente, A., Armandi, M., Fernandez, C., Garrone, E., Bonelli, B., 2012b. Thermal
641 collapse of single-walled alumino-silicate nanotubes: Transformation mechanisms and
642 morphology of the resulting lamellar phases. J. Phys. Chem. C 116, 23577–23584.
643 https://doi.org/10.1021/jp3090638

644 Zhou, L., Chen, Y.L., Zhang, X.H., Tian, F.M., Zu, Z.N., 2014. Zeolites developed from mixed
645 alkali modified coal fly ash for adsorption of volatile organic compounds. Mater. Lett. 119,
646 140–142. https://doi.org/10.1016/j.matlet.2013.12.097

647 Zhou, L., Zhang, X., Chen, Y., 2017. Modulated synthesis of zirconium metal–organic framework
648 UiO-66 with enhanced dichloromethane adsorption capacity. Mater. Lett. 197, 167–170.
649 https://doi.org/10.1016/j.matlet.2017.03.162

650

651


MCPA sorbed (μmol kg-1)
20000
15000
10000
5000
0
2
3
4
5
6
7
8
9
10
pH
Cl
O
O
O
+
ζ-potential (mV)
60
40
20
0
-20
-40
-60
2
4
6
8
10
12
pH